IEEE Access
Multidisciplinary | Rapid Review | Open Access Journal

Received 23 February 2023, accepted 13 March 2023, date of publication 16 March 2023, date of current version 30 March 2023.

Digital Object Identifier 10.1109/ACCESS.2023.3258040

RESEARCH ARTICLE

Design of 3D SAW Filters Based on the Spectral Element Method

YIWEN YAO[1], MINGWEI ZHUANG[1], (Member, IEEE), JUNHUI CHEN[1], KE CHEN[1], (Member, IEEE), AND QING HUO LIU[1,2], (Fellow, IEEE)

[1]Institute of Electromagnetics and Acoustics, Xiamen University, Xiamen 361005, China
[2]Eastern Institute for Advanced Study, Ningbo 315200, China

Corresponding authors: Mingwei Zhuang (mw.zhuang@xmu.edu.cn) and Qing Huo Liu (qhliu@eias.ac.cn)

This work was supported by the National Natural Science Foundation of China under Grant 61871462 and Grant 62101470.

ABSTRACT Surface acoustic wave (SAW) devices are key components in 5G communication systems, and the design of SAW filters with high frequency, high performance and high reliability is a necessary and challenging task. In this work, SAW resonators with $LiNbO_3/SiO_2/Si$ multi-layer structure are designed based on the spectral element method (SEM). Normally, however, massive computing resources are needed for solving a whole resonator directly by using full-wave numerical methods. To avoid simulating the large-aperture full structure of any SAW resonator, an equivalent small-aperture 3D structure can be modelled in the direction of the aperture by changing the internal resistance of the driving source to obtain the results of the full-scale aperture model. The one-port SAW resonators are then connected in the form of ladder networks to form band-pass SAW filters. The numerical results show that the SEM is more computationally efficient than the finite element method under the same number of degrees of freedom, and the results of the 3D small-aperture model are consistent with the complete resonator.

INDEX TERMS Spectral element method (SEM), resonator, SAW filter, aperture.

I. INTRODUCTION

Surface acoustic wave (SAW) devices have become key radio frequency (RF) devices in the wireless communication field. With the coming of 5G communications, and in order to meet the high performance demand of SAW devices, many new-type SAW devices with more complicated structures and multilayer piezoelectric substrates have been continuously developed, such as temperature compensated SAW devices [1], high-performance SAW devices on new substrates [2], heterogeneous acoustic layer SAW devices [3] and longitudinal leaky SAW devices [4]. However, for such SAW devices with complicated structures and high operating frequencies, an efficient technique for their accurate and fast simulation becomes a critical factor for device analyses and designs.

In modeling and simulation of SAW devices, several approximate but efficient methods have been widely utilized, including the delta function model [5], transmission matrices [6], equivalent circuit models [7], P-matrix model [8] and coupling-of-modes (COM) theory [9], but in general their accuracy is not sufficient for modeling the physical behaviors of SAW devices, especially when determining all the electromechanical effects and propagation characteristics [10], [11].

A rigorous technique for simulating a SAW device is to numerically solve the coupled partial differential equations (PDEs) governing the electric and mechanical fields, such as the finite element method (FEM), the boundary element method (BEM), and the combined FEM and BEM (FEM/BEM or FEBI). The FEM provides an effective and universal design evaluation, geometry independent resolution and the ability to seamlessly incorporate material losses (mechanical, electrodes and piezoelectric) and different boundary conditions [12], [13], [14]. In the BEM approach, a semi-infinite substrate can be rigorously modeled by the Green's function for the integral form of piezoelectric equations. The advantage of this approach is in accurate

The associate editor coordinating the review of this manuscript and approving it for publication was Guido Lombardi.

description of the substrate, as well as leaving a smaller region for the FEM analysis [15]. The FEBI method combines the advantages of the FEM and BEM methods and simulates the infinite SAW structure accurately [16], but the drawback of this approach is that it destroys the sparsity of the FEM system of equations [17], [18]. This leads to a significant increase in the computational cost that can be incompatible with short design time and cost effective computing system. In addition, a lot of care has to be taken to handle all singularities of the Green's function [19]. Up to now, a number of simulation techniques have been developed and applied to SAW modeling but there is still need for significant improvement.

The spectral element method (SEM) is a numerical technique with higher order accuracy for solving PDEs. This method combines the high accuracy and rapid convergence of the pseudo-spectral method and the geometrical flexibility those of the finite element method. Compared with the conventional FEM, SEM can save a large number of degrees of freedoms (DoFs) and improve the computational efficiency thanks to its fast convergence [20], [21]. Therefore, it is more computationally advantageous to simulate 3D SAW devices using the SEM.

In this paper, the 3D SAW model based on a multi-layer structure is built to obtain wave propagation responses. In general, a typical one port SAW resonator is on the order of 100 - 500λ long, 30 - 100λ wide in the lateral direction (aperture) and a depth of up to 100λ. Thus, it is nearly impossible to solve such large-scale model directly. To avoid simulating the whole SAW resonator, a finite small-aperture equivalent model can be utilized in 3D, by changing the internal resistance of driving source to obtain admittance or S-parameter of the actual large aperture. By comparing the numerical results from the whole 3D model with small-aperture model, we show that the simulation results can be in very close agreement with 3D-aperture model. The small-aperture used herein reduces the computer memory requirements and CPU time consumption. Additionally, this work establishes a coupled piezoelectrio-circuit model in which piezoelectrics are directly connected with an external electric circuit to calculate the current, voltage and power.

The rest of this paper is organized as follows: In section II, the SEM algorithm, a coupled piezoelectric-circuit model, small-aperture resonator and the modified Butterworth-Van Dyke (MBVD) models are described in detail. In section III, the accuracy of SEM algorithm and small aperture method is verified and the computational efficiency is compared through several calculation examples, and then the small aperture method is used to design high-order trapezoidal filters. Finally, a summary of the application of small aperture algorithm is drawn.

II. THEORY FOR SAW RESONATOR SIMULATION

A SAW resonator is based on electroacoustic multi-physical field effects to achieve the mutual conversion of electrical and acoustic energy. Figure 1 shows the vertical view

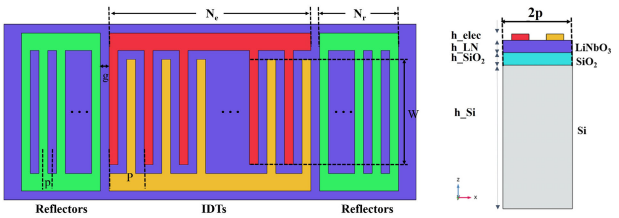

FIGURE 1. Schematic of a one-port resonator with key design parameters. (a) Top view. (b) Cross-sectional view.

of a typical SAW resonator on the piezoelectric substrate with key parameters labeled. The interdigital transducers are composed of N_e pairs of metal fingers with aperture W, pitch of electrodes P, and electrode width $P/4$. Two grating reflectors with N_r electrodes are placed at both sides of the interdigital transducers to enhance the acoustic wave reflection. The spacing p between reflective gratings composed of metal pairs is P/2, the gap g between IDT and reflective grating (GR) is set as P/4, and the metallization rate η is 0.5. Figure 1(b) shows the cross-sectional view of the three-layer model with $LiNbO_3$(lithium niobate), SiO_2 and Si. Among them, the thicknesses of lithium niobate, SiO_2 and electrodes are sub-wavelength and given as 0.175P, 0.175P and 0.0125P, respectively. Silicon is used as the substrate, and its thickness is set to 6P, and PML is used at its bottom to absorb outgoing waves. Under the time convention of $e^{-i\omega t}$, the propagation of the acoustic waves in a piezoelectric material is governed by the following coupled electromechanical equations:

$$\rho\omega^2\boldsymbol{u} + \nabla\cdot\boldsymbol{\tau} = 0 \tag{1}$$

$$\nabla\cdot\boldsymbol{D} = \rho_e \tag{2}$$

$$\boldsymbol{\tau} = \boldsymbol{c}:\boldsymbol{\varepsilon} - \boldsymbol{e}\cdot\boldsymbol{E} \tag{3}$$

$$\boldsymbol{D} = \boldsymbol{e}:\boldsymbol{\varepsilon} + \boldsymbol{\epsilon}\cdot\boldsymbol{E} \tag{4}$$

$$\boldsymbol{E} = -\nabla V \tag{5}$$

$$\boldsymbol{\varepsilon} = \frac{1}{2}(\nabla\boldsymbol{u} + \nabla\boldsymbol{u}^{\boldsymbol{T}}) \tag{6}$$

where ρ, $\boldsymbol{u}$, $\boldsymbol{\tau}$ and $\boldsymbol{\varepsilon}$ are the mass density, displacement vector, stress tensor and strain tensor, respectively. $\boldsymbol{D}$, $\boldsymbol{E}$, V and ρ_e are the electric displacement, electric field, voltage and applied charge density, respectively. $\boldsymbol{\epsilon}$, $\boldsymbol{e}$, and $\boldsymbol{c}$ are the second-order dielectric constant, third-order piezoelectric coupling coefficient and fourth-order elastic matrix, respectively. The constitutive equations (3) and (4) realize the linear electromechanical interaction between the mechanical and electrical states in piezoelectric materials. For non-piezoelectric materials(Si, SiO_2), however, the piezoelectric coupling coefficient will vanish, and there is no coupling effect between mechanical and electrical energy.

To solve the piezoelectric equations with the SEM, it is necessary to convert equation (1) and equation (2) into weak forms by multiplying, both sides of the equations by the test function w and integrating it, and then using the integration

by parts to yield.

$$-\omega^2 \int_\Omega w\rho \boldsymbol{u} d\Omega = \int_\Gamma w\hat{n} \cdot \boldsymbol{\tau} d\Gamma - \int_\Omega \nabla w \cdot \boldsymbol{\tau} d\Omega \quad (7)$$

$$\int_\Omega w\rho_e d\Omega = \int_\Gamma w\hat{n} \cdot \boldsymbol{D} d\Gamma - \int_\Omega \nabla w \cdot \boldsymbol{D} d\Omega \quad (8)$$

In the above, Ω is the whole computational domain, Γ is its boundary surface, $\hat{n}$ is the unit normal direction of the boundary surface, and w is the test function. In the weak form formulation, the computation domain Ω will be divided into K non-overlapping hexahedral elements. Each hexahedral element in the physical space will be mapped to the reference cubic element through coordinate transformation, so that the numerical integration, derivation and interpolation can be directly carried out in the reference element. The spectral element method in this work uses the Legrange function as the basis functions, and selects the Gauss-Lobatto-Legendre (GLL) points as the interpolation points. In the reference element, the Nth-order basis function has $N+1$ GLL points, defined as:

$$\phi_i^N(\xi) = \frac{-1}{N(N+1)L_N(\xi_i)} \frac{(1-\xi^2)L_N'(\xi_i)}{\xi - \xi_i} \quad (9)$$

where $\xi \in [-1, 1]$, $i = 1, \cdots, N+1$, $L_N(\xi_i)$ and $L_N'(\xi_i)$ are the Nth-order Legendre polynomial and its derivative, respectively. So in the three-dimensional problem, the physical field will be expanded using these basis functions. For example, the x component of the displacement field is:

$$u_x(\xi, \eta, \gamma) = \sum_i^{N_\xi} \sum_j^{N_\eta} \sum_k^{N_\gamma} u_x(\xi_i, \eta_j, \gamma_k) \times \phi_i^N(\xi)\phi_j^N(\eta)\phi_k^N(\gamma) \quad (10)$$

and similarly for other displacement components and for the electrical potential. Boundary conditions at the outer surface will involve the displacement vector ($\boldsymbol{u}$), the electrical potential (V), the normal components of the stress ($\hat{n} \cdot \tau|_\Gamma$) and of the electrical displacement ($\hat{n} \cdot \boldsymbol{D}|_\Gamma$). Firstly, stress-free boundary conditions ($\hat{n} \cdot \tau|_\Gamma = 0$, the surface traction is zero) is applied to the top of the substrate and electrodes. Secondly, the perfectly matched layer (PML) boundary condition is applied to eliminate the spurious reflections at the bottom of the substrate. Finally, the electric signal boundary conditions are imposed on the electrodes and the outer insulator surfaces. Each SAW resonator is made up of periodic interdigital electrodes connected to two bus bars which connect to the electrical source (or load). Therefore, a coupled piezoelectro-circuit model needs to be established in electric boundary conditions, in which piezoelectrics are directly connected with an external electric circuit to calculate the current, voltage and power. It is important to note that the boundary integrate for quasi-static equation will generate electric charge Q on the surface of the electrodes, i.e. $Q = \int_\Gamma wn \cdot \boldsymbol{D} d\Gamma$. The current routed through the electrodes are

$$I = \quad -i\omega Q = -i\omega \int_\Gamma w\hat{n} \cdot \boldsymbol{D} d\Gamma \quad (11)$$

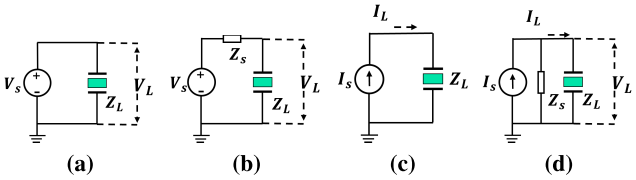

FIGURE 2. Four typical circuit models for piezoelectro-circuit systems. (a) Ideal voltage source V_s; (b) Voltage source V_s with an internal impedance Z_s; (c) Ideal current source I_s; (d) Current source I_s with an internal impedance.

Four typical models designed and implemented in Figure 2, and the relationships between voltage source (or current source) and SAW resonator are shown below:

- Ideal voltage source:

$$V|_\Gamma = V_s \quad (12)$$

- Voltage source with an internal impedance :

$$\int_\Gamma w\hat{n} \cdot \boldsymbol{D} d\Gamma = -I_L/i\omega = -(V_s - V|_\Gamma)/i\omega Z_s \quad (13)$$

- Ideal current source:

$$\int_\Gamma w\hat{n} \cdot \boldsymbol{D} d\Gamma = -I_L/i\omega = -I_s/i\omega \quad (14)$$

- Current source with an internal impedance:

$$\int_\Gamma w\hat{n} \cdot \boldsymbol{D} d\Gamma = -I_L/i\omega = -(I_s Z_s - V|_\Gamma)/i\omega Z_s \quad (15)$$

where V_s and $V|_\Gamma$ are the voltages at the voltage source and electrode, respectively; I_s and I_L are the currents at the current source and load, respectively; Z_s is the internal impedance of the source. The voltage of the electrode $V|_\Gamma$ is unknown except for ideal voltage source. Special attention must be paid for the simple RCL circuit, where Z_s is a complex number. In addition, if the electrode is directly connected with a load resistor, the voltage V_s is zero in equation (13).

For the conventional 3D SEM, the substitution of the polynomial interpolation equation (10) and boundary conditions equations (12)-(15) into equation (7)-(8), the system matrix equation can be written as

$$\begin{pmatrix} \mathbf{K}^{uu} + j\omega\mathbf{C}^{uu} - \omega^2\mathbf{M}^{uu} & \mathbf{K}^{uV} \\ \mathbf{K}^{Vu} & -\mathbf{K}^{VV} \end{pmatrix} \begin{pmatrix} \mathbf{u} \\ \mathbf{V} \end{pmatrix} = \begin{pmatrix} 0 \\ f_e \end{pmatrix} \quad (16)$$

where $\mathbf{M}^{uu}$ is the mechanical mass matrix, $\mathbf{C}^{uu}$ is the mechanical damping matrix, $\mathbf{K}^{uV}$ is the piezoelectric coupling matrix, $\mathbf{K}^{uu}$ and $\mathbf{K}^{VV}$ are the mechanical and dielectric stiffness matrices, respectively, and f_e is the electric charge vector. An iterative or direct solver is used to solve the above linear system.

A typical SAW resonator is on the order 30λ - 100λ wide in the aperture direction, and it is nearly impossible to simulate such large-scale aperture directly using a full-wave solver in 3D. Therefore, one usually use a simplified but equivalent resonator with a finite small-aperture grating in simulation, and the numerical results are in consonance with the actual-aperture resonator. As is well known, the displacement field

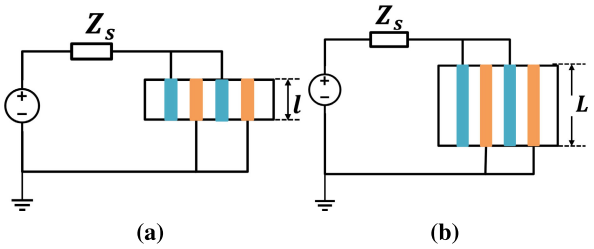

FIGURE 3. The schematic diagram of power supply simulation for (a) small aperture model with an aperture length of ℓ. and (b) a large aperture model with an aperture length of L.

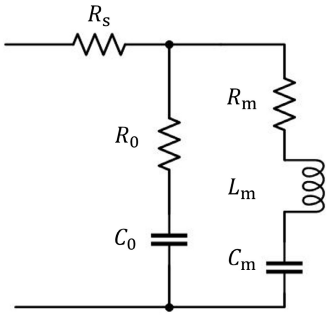

FIGURE 4. The modified Butterworth-Van Dyke (MBVD) circuit as an equivalent circuit of the SAW resonator.

and electric field form an equiphase plane along the aperture direction if the fringe effects at both ends of the aperture are neglected. The current is obtained by integrating normal electric displacement on the aperture surface, and the integral in equation (11) is proportional to the electrode width (acoustic aperture) when the electrode length is fixed. Thus, the impedance of the resonator is inversely proportional to the area of cross-section. As shown in Figure 3, the currents routed through the electrodes are equation (11). The current relationships between the small-aperture (l) and large-aperture (L) are

$$I_L = \alpha I_l = \frac{V_s - V|_\Gamma}{Z_L} \tag{17}$$

$$I_l = \frac{V_s - V|_\Gamma}{Z_l} \tag{18}$$

where α is the ratio of the large aperture to small aperture, Z_l and Z_L are the impedance modulus connecting the small aperture and large aperture model, respectively. So, the SAW resonator with large-scale aperture can be achieved and only by changing the internal resistance Z_l in the finite small-aperture resonator, i.e. $Z_l = \alpha Z_L$. Then, for a finite small-aperture resonator, the voltage and current in electrodes are equivalent to those in a real-aperture model.

Through the voltage and current, the admittance response of the SAW resonator including the resonance frequency and anti-resonance frequency can be obtained. The modified Butterworth-Van Dyke (MBVD) model has been used as an equivalent circuit of the SAW resonator to extract relevant parameters [22], [23], as shown in Figure 4. The relationships between the circuit parameters are expressed as

$$C_0 = \frac{1}{n}\sum_{i=1}^{n}\frac{1}{imag(Z_i)2\pi f_i} \tag{19}$$

$$C_m = C_0[(\frac{\omega_p}{\omega_s})^2 - 1] \tag{20}$$

$$L_m = \frac{1}{\omega_s^2 C_m} \tag{21}$$

$$R_m = \frac{\omega_s L_m}{Q_s} \tag{22}$$

$$R_0 = (\frac{\omega_p}{\omega_s}\frac{Q_s}{Q_p} - 1) \tag{23}$$

$$R_s = (\frac{Q_s}{Q_{s0}} - 1)R_m \tag{24}$$

where C_0 is the static capacitance and represents the capacitance between the electrodes and the substrates, and it can be estimated by selecting the impedance values $Z_i = Z(\omega_i)$, $i = 1, \cdots, n$ at n (usually 5-10) frequency points away from the resonance frequency; ω_p and ω_s are the parallel resonant frequency and the series resonant frequency, respectively; C_m, L_m and R_m are motional capacitance, inductance and resistance, respectively; R_s models the resistance of the electrodes, while R_0 helps for better description of acoustic losses when the circuit is in parallel resonance. The acoustic resistor R_m also models acoustic losses which affects predominately the series resonance. Q_p, Q_s and Q_{s0} are quality factor of the parallel resonance, quality factor of the series circuit $R_m L_m C_m$ and quality factor of the series resonance for the whole circuit including resistors R_s, respectively. The approach for determining Q_{s0} and Q_p is to use the slope of the phase characteristic of the impedance. The value of Q_s cannot be obtained directly due to the existence of R_s, so it is necessary to estimate Q_s firstly and then correct it (detailed description in [22]). The admittance response obtained by the parameters estimated by the above formulas will have a certain error with the SEM analysis result, but the parameters can be optimized by ADS. The MBVD models have been used for the design and optimization of topologies of SAW filters including π-shaped, T-shaped, and ladder filters, etc.

III. NUMERICAL EXAMPLES

In this section, a wideband SAW resonator in a $LiNbO_3/SiO_2/Si$ layered structure [24] is used to illustrate the accuracy of the SEM, and the finite-element solutions are used as references. The thickness of $LiNbO_3$, SiO_2, Si and electrode are provided in Table 1, and the material parameters are given in the Appendix. The piezoelectric material $LiNbO_3$ substate have Euler angles (0°, 60°, 120°) and its material parameters are also given in the Appendix.

A. A PAIR ELECTRODE RESONATOR

We first consider a pair electrode model to investigate the accuracy of the SEM algorithm, as shown in figure 1(b).

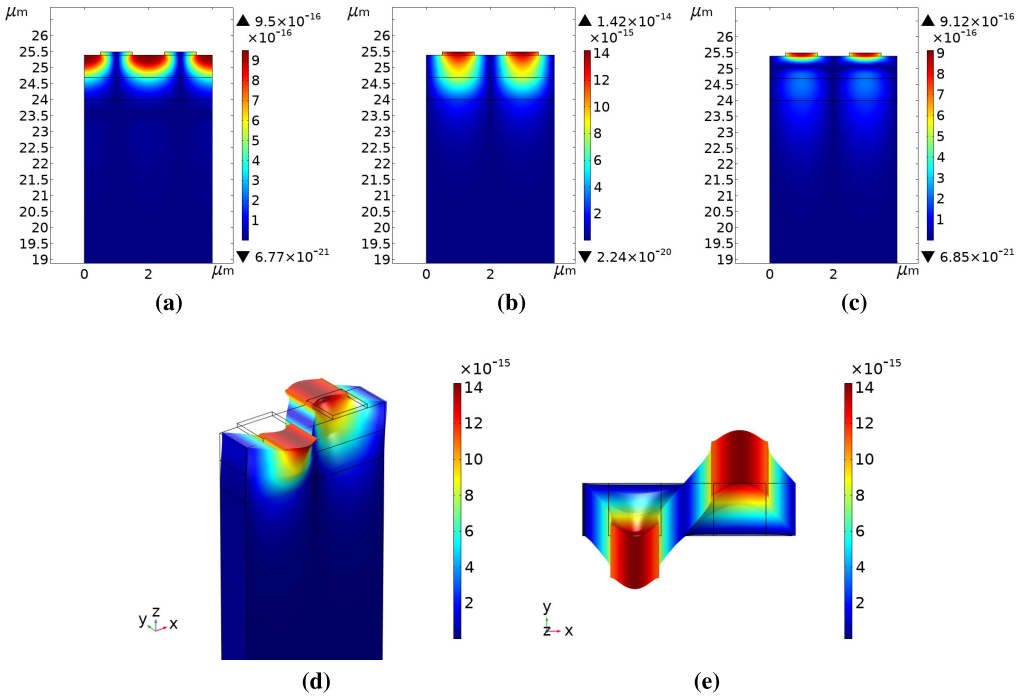

FIGURE 5. Displacement field distribution with frequency of 808 MHz along the cut plane X=0.3 μm for the single pair of electrode of P=4 μm, (a) amplitude of u_x, (b) amplitude of u_y, (c) amplitude of u_z, (d) 3D simulated SH vibration displacement distribution. (e) Displacement distribution diagram on the XZ plane.

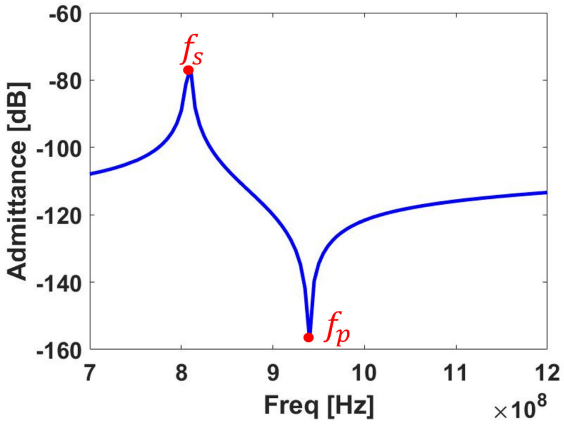

FIGURE 6. Simulated admittance response of SH-SAW resonator with P=4 μm.

A periodic boundary is used in the x- and y-direction, and the bottom of the Si substrate is a PML. Applying a 1V voltage with internal resistance 50 Ω to input electrodes, and the output electrodes are connected to ground. The measured voltages generated on the input and output electrodes are used to calculate the frequency response of the SAW resonator. For the resonator structure shown in Figure 1(b), in order to transmit SH-SAW with high electromechanical coupling coefficient k^2, the thickness of lithium niobate film, silicon dioxide and electrodes and the electrode material need to be optimized. In [24] and [25], k^2 of SH-SAW resonator exceeds 45% at h_{LN}/P of 0.2-0.25 with Au-IDT of 0.025P thick and h_{LN} is equal to h_{SiO_2}. When solving the periodic single pair of electrodes with P = 4 μm, it is found that resonance occurs at f_s = 808 MHz. As shown in Figure 5, the shear horizontal surface acoustic wave propagating on the lithium niobate piezoelectric film mainly focuses on the piezoelectric layer due to the LN/SiO_2 acoustic waveguide structure. Figure 5(d) shows the simulated displacement distribution when the SH-SAW wave propagates along the x direction. The vibration displacements are parallel to the substrate along the y direction. According to the admittance response in Figure 6, it can be concluded that the electromechanical coupling coefficient of SH-SAW resonator designed based on LNOI structure with P=4 μm can reach 42% according to $k^2 = \pi^2/8 \times (f_p^2 - f_s)^2/f_s^2$, where f_s and f_p are resonant and antiresonant frequencies, respectively.

The mesh used for the SEM and FEM numerical simulation are composed of 8200 hexahedron elements, and the degree of freedom of the mesh is about 796,120. As show in figure 7 and 8, the calculated displacement waveforms and voltage from the SEM method is compared with the FEM solutions in 900 MHz. It is shown that excellent agreement is achieved for the two numerical solutions. The L_2 norm errors of the SEM and FEM solutions are 0.65% and 0.3%, respectively.

In order to validate the efficiency of the SEM solver, the frequency response of the SAW resonator at different pitch values of P of electrodes are calculated over the frequency band from 700 MHZ to 1400 MHz with 140 frequency points. The simulated admittance of the SAW resonator is provided

TABLE 1. Key model parameters of single pair of electrodes.

Symbol	value	Descripition
P	4 μm, 3.7 μm, 3.5 μm, 3.2 μm	IDT Period
h_{LN}	0.175P	LN thickness
h_{SiO_2}	0.175P	SiO_2 thickness
h_{Si}	6P	Si thickness
h_{elec}	0.0125P	Electrode thickness
η	0.5	mentalization ratio
3D section	(0, 0.3, 25.05), (4, 0.3, 25.05)	Coordinates of 3D section line

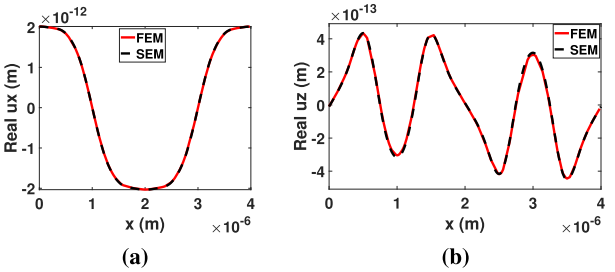

FIGURE 7. Displacement on the three-dimensional section line obtained by SEM, FEM. (a) Real part of displacement in the *x* direction, (b) Real part of displacement in the *z* direction.

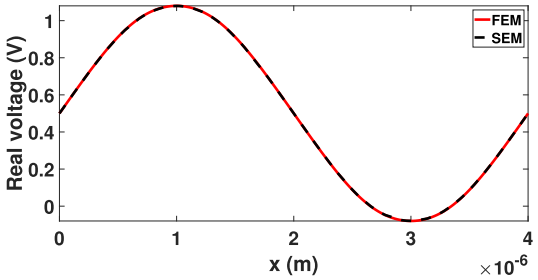

FIGURE 8. Voltage comparison on a 3D cross-section between SEM and FEM in the x direction.

in Figure 9 with different pitch values. SEM takes only 1.1h to complete all simulations, while the FEM in COMSOL takes about 1.5h. The efficiency has increased by around 1.4 times by using SEM, which is a significant improvement, particularly for large-scale models that actually need to be simulated.

B. LARGE-SCALE APERTURE RESONATOR

In the previous section, a single-pair electrode model was used to compare the computational results of SEM and FEM. In this section, a more complex structure will be used to compare the results of SEM and FEM for the full-scale structure. The SAW resonator is configured with IDTs consisting of 20 pairs of fingers and 10 grating reflectors placed on both sides of the IDTs, and the aperture length is 21 μm. The operating IDT period P is set as 3.5 μm. It is noted that in order to prevent the required computer resources of the complete

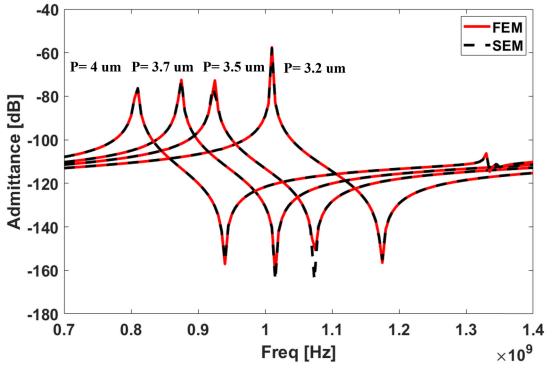

FIGURE 9. Comparison of admittance responses from SEM and FEM at different pitches.

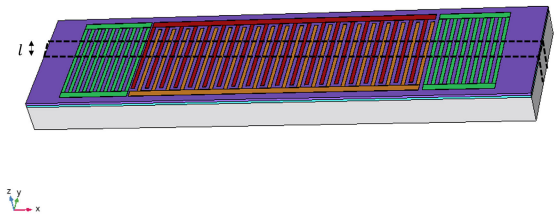

FIGURE 10. Schematic diagram of 3D model of large aperture resonator.

resonator from being too large, the thickness of *Si* is adjusted from 6P to 2P. Figure 10 shows the full 3D model. The structure with aperture length l of 2 μm is selected, and the periodic boundary condition is adopted at the y-axis boundary. In order to better compare the displacement changes of the SH-SAW resonator under the three-dimensional structure when the SH wave propagates in the x direction, the 3D section line from (0, 0.1, 8.0) to (120, 0.1, 8.0) at frequency $f = 1$ GHz is selected to observe the displacement change of the resonator in the piezoelectric layer of lithium niobate. Figure 11 shows the displacement under this cross-section as SH-SAW propagates along the x direction at frequency $f = 1$ GHz. It is shown that excellent agreement is achieved for the two numerical solutions. For the real part of u_x, u_y and u_z component, the L_2 norm errors of the SEM and FEM solutions referring the FEM results are 2%, 1% and 1%, respectively.

The accuracy of the equivalent resistance theory using the finite small-aperture model was validated by comparing its results with the actual large-aperture model with full size. It is noted that the aperture just needs to be discretized by one hexahedral element (i.e.,0.2 μm) for finite small-aperture model, and periodic boundary are used in the aperture (y) direction. If a 1V voltage source with internal resistance 50 Ω is applied to the large-aperture model, the internal resistance will be adjusted to 50α Ω (α=105) in the equivalent

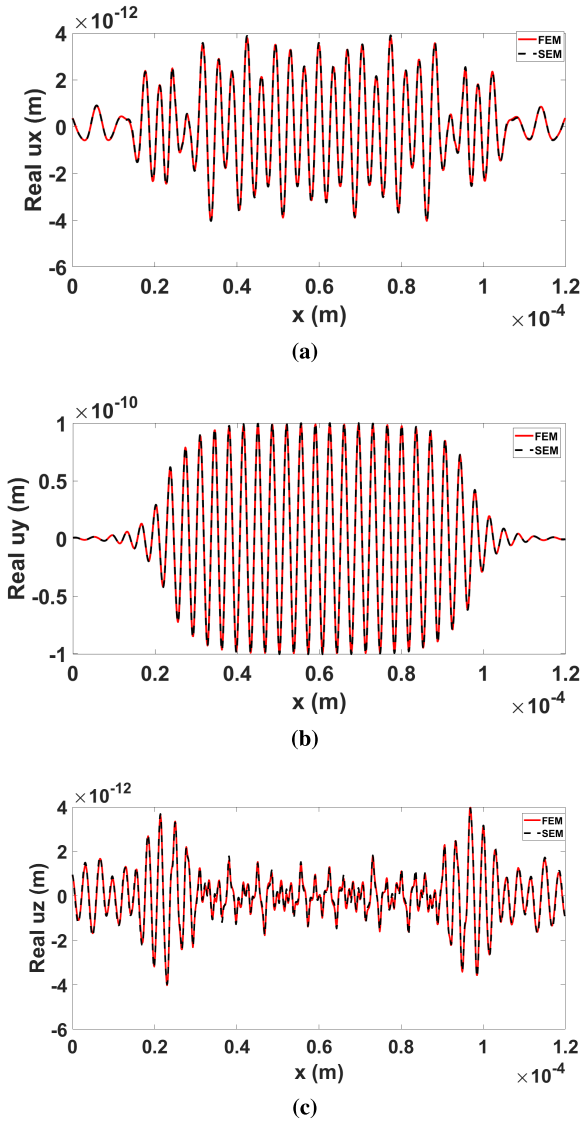

FIGURE 11. Displacement on the three-dimensional section line in Figure 10 obtained by SEM and FEM at f=1 GHz. (a) Real part of u_x component, (b) Real part of u_y component. (c) Real part of u_z component.

finite small-aperture model. Thus, the number of degrees of freedom of the mesh is 3.1 million and 17.9 million for small- and large-aperture models, respectively. The simulated admittance of the resonator is provided in Figure 12 for the finite small-aperture model, large-aperture model without the fringe effects and large-aperture model with the fringe effects. It is noted that the number of degrees of freedom of the large-aperture model is very large, thus consuming a large amount of computer resources, so only dozens of frequency points were compared. As shown in Figure 12, the admittance has excellent agreement with the large-aperture model if the fringe effects at both ends of aperture are neglected. For the large-aperture model with fringe effects, however, the acoustic signals were reflected from the aperture fringes, but the admittance results are also consistent with the finite

TABLE 2. SEM calculation details of small aperture structure, large aperture structure and two-dimensional structure COMSOL calculation details.

Model	DoFs (million)	PPW	Frequency points	Time	order
Small aperture	3.1	9	140	1 h	3
Large aperture	17.9	7	35	48 h	3
2D model	0.93	9	140	0.6 h	3

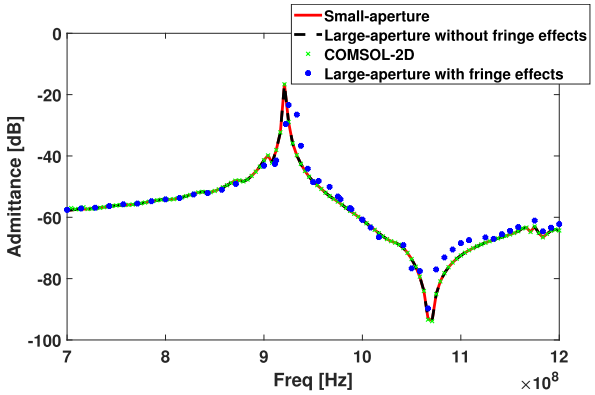

FIGURE 12. Comparison of admittance responses among the finite small-aperture structure, large-aperture structure without the fringe effects, 2D structure of COMSOL and large-aperture structure with the fringe effects for the model in Figure 10.

small-aperture. Therefore, the simulation of a large-aperture resonator can degenerate into a small-aperture model.

COMSOL software has been widely applied as a powerful tool for analyzing the wave-acoustic process in piezoelectric crystals. Compared with two-dimensional calculations, three-dimensional calculations will require more DoFs. While comparing the computational efficiency of large aperture and small aperture under SEM, the computational efficiency of COMSOL in 2D is added. As shown in Figure 12, the admittance response of the 2D structure has excellent agreement with the small-aperture model and the large-aperture model neglecting the fringe effects. And the L_2 norm errors of the 2D structure of COMSOL and small-aperture of SEM solutions is 4%. As shown in table 2, the number of DoFs of the 3D small-aperture model is about 3 times that of 2D model, and the calculation time of SEM is only about twice that of COMSOL in 2D. It shows that the small aperture model using SEM has computational advantages in 3D.

C. SAW FILTER DESIGN

In the previous part, the accuracy of the algorithm is verified by comparing the results of the full-wave simulation and the finite small-aperture model. In this part, the small aperture model is used to calculate the series and parallel resonators and design the high-order ladder filter based on the simulation results. In order to obtain a larger bandwidth of the trapezoidal filter, the frequency offset between the resonant

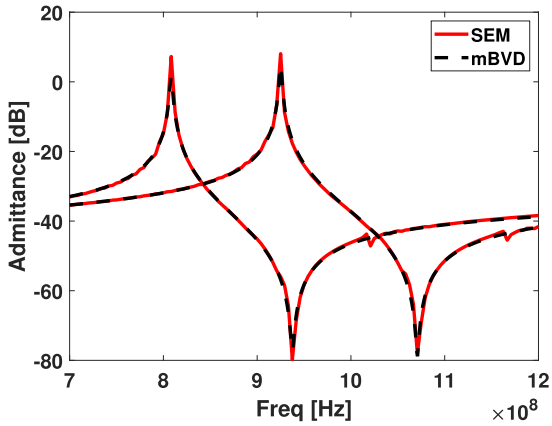

FIGURE 13. Comparison of admittance response between MBVD-circuit and small aperture SEM method.

TABLE 3. Extracted parameters of shunt and series resonator.

parameter	f_s (MHz)	k^2 (%)	L_m (nH)	R_m (Ω)	C_m (pF)	C_0 (pF)	R_0 (Ω)	R_s (Ω)
Shunt	808	42.71	52.1	0.58	0.744	2.15	0	0.15
Series	925	41.96	40.5	0.59	0.73	2.15	0	0.25

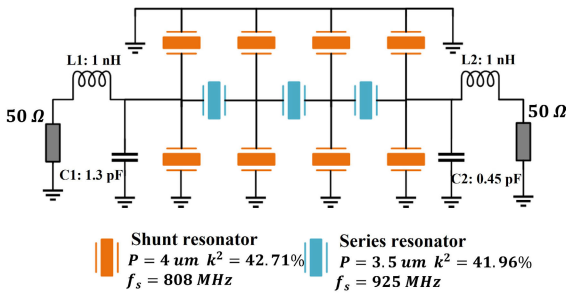

FIGURE 14. Topology of high order filter and resonators parameters.

frequencies of the series resonator and the parallel resonator is carefully designed. Referring to the simulation design of the single-pair electrode SAW resonator device in the subsection III-B, the pitches of the series and parallel resonators are 4 μm and 3.5 μm, respectively. The length of the small aperture model W is 0.2 μm, and the corresponding complete model is 70 pairs of IDT, 20 pairs of reflection gratings, and the length of the acoustic aperture is 20 wavelengths. Refer to Figure 1 and Figure 10 for the simulated 3D model view. Figure 13 shows the admittance response of the designed series and parallel resonators. The MBVD circuit parameters of the series and parallel resonators are extracted from equations (19)-(24) explicitly. The relevant parameters are listed in Table 4. As shown in Figure 13, the MBVD circuit result is in good agreement with the SEM simulation results if some spurious waves are ignored. Due to the existence of Rayleigh waves around 1.2 GHz in the simulation results, the equivalent MBVD circuit cannot obtain such a waveform, but

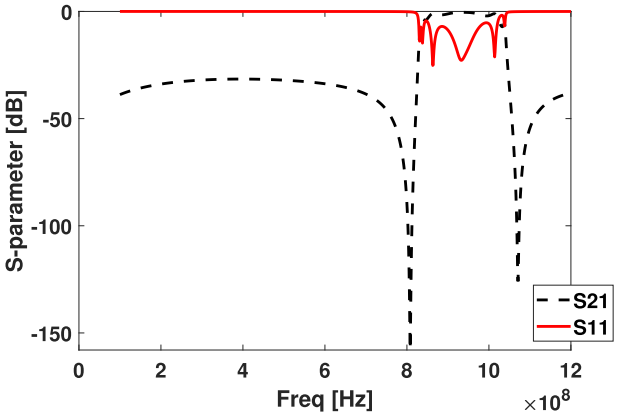

FIGURE 15. S-parameters (S11 and S21) of the high order filter.

TABLE 4. Elastic material.

material	Density (Kg/m^3)	Young modulus (Pa)	Possion ratio
Si	2320	160e9	0.22
Au	19300	70e9	0.44
SiO_2	2320	70e9	0.17

this does not affect the filter design in the frequency band. The structure of traditional trapezoidal filter is composed of the series resonators and parallel resonators. The higher the order of the ladder filter, the better the out-of-band suppression will be, and the insertion loss of the passband will also be reduced. There must be a trade-off when building a topology circuit. In the design of the ladder filter architecture, various topological structures have been investigated, and the simulation results showed that the structure in [26] produced higher out-of-band rejection and lower insertion loss. In order to obtain a high out-of-band suppression effect, a "sixth-order" ladder filter is designed. And a parallel resonator is added to the input and output ends of the traditional sixth-order ladder filter respectively. This kind of trapezoidal filter has better out-of-band suppression effect than the seventh-order trapezoidal filter, and the insertion loss will not deteriorate, which is also beneficial to the flatness in the band. As shown in Figure 14, the standard impedance is 50 Ω, and matching circuits are added to the input and output ports. The simulated S-parameters of the trapezoidal filter are shown in Figure 15. Using the simulation results of this equivalent admittance algorithm to build the variation trend of the S parameters of the circuit, it can be seen that this simulation has indeed achieved good filtering effects. Figure 15 shows that the out-of-band suppression is below −40 dB and insertion loss is less than 2.0 dB, indicating that the equivalent admittance calculation method of the small aperture model in accurate while reducing the computational costs.

IV. CONCLUSION

In this study, the spectral element technique has developed for simulation of 3D SAW resonator. A coupled

piezoelectric-circuit model was established, in which the electrodes were directly connected with an external electric circuit to calculate the current, voltage and admittance. In addition, admittance of a large-aperture grating can be modeling via equivalent resistance method. Using the approach described the admittances of resonator with small- and large-aperture are entirely coincident. Our results show that the SEM used herein reduces the computation requirements and time consumption while maintaining sufficient accuracy for the SAW resonator. Finally, using this method to design a ladder filter with the insertion loss of less than 2.0 dB and the bandwidth of 145 MHz shows the practicability of the algorithm. It shows that SEM of the small aperture model proposed in this work can accurately simulate the surface acoustic wave characteristics of the complete model SAW device, and the simulation efficiency is greatly improved.

APPENDIX. MATERIAL CONSTANTS

Lithium niobate ($LiNbO_3$):

$\rho = 4650\,Kg/m^3$

$$C_{ij} = \begin{bmatrix} 2.0 & 0.543 & 0.70 & 0.079 & 0 & 0 \\ 0.543 & 2 & 0.70 & -0.079 & 0 & 0 \\ 0.70 & 0.70 & 2.424 & 0 & 0 & 0 \\ 0.079 & -0.079 & 0 & 0.595 & 0 & 0 \\ 0 & 0 & 0 & 0 & 0.595 & 0.079 \\ 0 & 0 & 0 & 0 & 0.079 & 0.0728 \end{bmatrix} \times 10^{11}\,N/m^2$$

$$e_{ij} = \begin{bmatrix} 0 & 0 & 0 & 0 & 3.7 & -2.38 \\ -2.38 & 2.38 & 0 & 3.7 & 0 & 0 \\ 0.34 & 0.34 & 1.6 & 0 & 0 & 0 \end{bmatrix} C/m^2$$

$$\epsilon_{ij} = \begin{bmatrix} 44.3 & 0 & 0 \\ 0 & 44.3 & 0 \\ 0 & 0 & 27.9 \end{bmatrix}$$

REFERENCES

[1] R. Ruby, S. Gilbert, S. K. Lee, J. Nilchi, and S. W. Kim, "Novel temperature-compensated, silicon SAW design for filter integration," *IEEE Microw. Wireless Compon. Lett.*, vol. 31, no. 6, pp. 674–677, Jun. 2021.

[2] T. Takai, H. Iwamoto, Y. Takamine, H. Yamazaki, T. Fuyutsume, H. Kyoya, T. Nakao, H. Kando, M. Hiramoto, T. Toi, M. Koshino, and N. Nakajima, "High-performance SAW resonator on new multilayered substrate using LiTaO3Crystal," *IEEE Trans. Ultrason., Ferroelectr., Freq. Control*, vol. 64, no. 9, pp. 1382–1389, Sep. 2017.

[3] H. Zhou, S. Zhan, P. Zheng, L. Zhang, J. Wu, H. Yao, T. You, and X. Ou, "A 6.1 GHz wideband solidly-mounted acoustic filter on heterogeneous substrate for 5G front-ends," in *Proc. IEEE 35th Int. Conf. Micro Electro Mech. Syst. Conf. (MEMS)*, Jan. 2022, pp. 1006–1009.

[4] M. Suzuki and S. Kakio, "Theoretical analysis and design of longitudinal leaky SAW device consisting of ScA1N film/piezoelectric single crystal substrate," in *Proc. IEEE Int. Ultrason. Symp. (IUS)*, Oct. 2018, pp. 1–9.

[5] K.-Y. Hashimoto and M. Yamaguchi, "Delta function model analysis of SSBW spurious responses in SAW devices," *Electron. Commun. Jpn., III, Fundam. Electron. Sci.*, vol. 76, no. 8, pp. 37–44, 1993.

[6] C. K. Campbell, "Scattering and transmission matrix analysis of SAW resonator filters with long-pair IDTs and triple composite longitudinal modes on quartz," in *Proc. IEEE Ultrason. Symp.*, vol. 1, Oct. 1994, pp. 309–312.

[7] N. J. Mukhtar, N. A. Aziz, B. Bais, and B. Y. Majlis, "Circuit modeling of surface acoustic wave (SAW) resonator with circular geometry," in *Proc. IEEE Int. Conf. Semiconductor Electron. (ICSE)*, Aug. 2016, pp. 57–60.

[8] A. N. Rusakov, "Modified P-matrix model and its implementation for design of SAW resonator filters," in *Proc. IEEE Ultrason. Symp.*, vol. 1, Aug. 2004, pp. 85–89.

[9] Y.-M. Zhang, J. Jin, H.-L. Li, and H.-P. Hu, "A novel method to extract COM parameters for SAW based on FEM," in *Proc. 13th Symp. Piezoelectrcity, Acoustic Waves Device Appl. (SPAWDA)*, Jan. 2019, pp. 1–5.

[10] K. Yamanouchi, K. Kotani, H. Odagawa, and Y. Cho, "Theoretical analysis of SAW propagation characteristics under the strained medium and applications for high temperature stable high coupling SAW substrates," in *Proc. IEEE Ultrason. Symp.*, Oct. 1999, pp. 239–242.

[11] K. Yamanouchi and A. Ishii, "High temperature stable super high electromechanical coupling SAW substrates and application for SAW devices," in *Proc. IEEE Int. Freq. Control Symp. PDA Exhib.*, May 2002, pp. 66–69.

[12] B. Zhang and H. Hu, "A FEM simulation approach for multilayered SAW delay line devices," in *Proc. IEEE Int. Conf. Robot. Biomimetics (ROBIO)*, Dec. 2015, pp. 970–975.

[13] S. Ballandras, R. Lardat, M. Wilm, T. Pastureaud, A. Reinhardt, N. Champavert, W. Steichen, W. Daniau, V. Laude, R. Armati, and G. Martin, "A mixed finite element/boundary element approach to simulate complex guided elastic wave periodic transducers," *J. Appl. Phys.*, vol. 105, no. 1, Jan. 2009, Art. no. 014911.

[14] A. Iyama, X. Li, J. Bao, N. Matsuoka, T. Omori, and K.-Y. Hashimoto, "Full 3D FEM analysis of scattering at a border between IDT and reflector in SAW resonators," in *Proc. IEEE Int. Ultrason. Symp. (IUS)*, Oct. 2019, pp. 1235–1238.

[15] A. Tajic, A. Volatier, R. Aigner, and M. Solal, "Simulation of solidly mounted BAW resonators using FEM combined with BEM and/or PML," in *Proc. IEEE Int. Ultrason. Symp.*, Oct. 2010, pp. 181–184.

[16] M. Solal, L. Chen, and J. Gratier, "Measurement and FEM/BEM simulation of transverse effects in SAW resonators on lithium tantalate," *IEEE Trans. Ultrason., Ferroelectr., Freq. Control*, vol. 60, no. 11, pp. 2404–2413, Nov. 2013.

[17] M. Solal, T. Abboud, S. Ballandras, S. Chamaly, V. Laude, R. Lardat, T. Pastureaud, J. Ribbe, W. Steichen, and P. Ventura, "FEM/BEM analysis for SAW devices," in *Proc. 2nd Int. Symp. Acoustic Wave Devices Future Mobile Commun. Syst.*, 2004, pp. 185–202.

[18] V. Laude, A. Reinhardt, M. Wilm, A. Khelif, and S. Ballandras, "Fast FEM/BEM simulation of SAW devices via asymptotic waveform evaluation," *IEEE Trans. Ultrason., Ferroelectr., Freq. Control*, vol. 51, no. 3, pp. 359–363, Mar. 2004.

[19] P. Ventura, J. M. Hode, J. Desbois, and H. Solal, "Combined FEM and green's function analysis of periodic SAW structure, application to the calculation of reflection and scattering parameters," *IEEE Trans. Ultrason., Ferroelectr., Freq. Control*, vol. 48, no. 5, pp. 1259–1274, Sep. 2001.

[20] L. Shi, Y. Zhou, J.-M. Wang, M. Zhuang, N. Liu, and Q. H. Liu, "Spectral element method for elastic and acoustic waves in frequency domain," *J. Comput. Phys.*, vol. 327, pp. 19–38, Dec. 2016.

[21] M. Zhuang, Q. Zhan, J. Zhou, Z. Guo, N. Liu, and Q. H. Liu, "A simple implementation of PML for second-order elastic wave equations," *Comput. Phys. Commun.*, vol. 246, Jan. 2020, Art. no. 106867.

[22] I. S. Uzunov, M. D. Terzieva, B. M. Nikolova, and D. G. Gaydazhiev, "Extraction of modified Butterworth—Van Dyke model of FBAR based on FEM analysis," in *Proc. Int. Sci. Conf. Electron. (ET)*, Sep. 2017, pp. 1–4.

[23] R. Lu, M.-H. Li, Y. Yang, T. Manzaneque, and S. Gong, "Accurate extraction of large electromechanical coupling in piezoelectric MEMS resonators," *J. Microelectromech. Syst.*, vol. 28, no. 2, pp. 209–218, Apr. 2019.

[24] T.-H. Hsu, K.-J. Tseng, and M.-H. Li, "Large coupling acoustic wave resonators based on $LiNbO_3/SiO_2/Si$ functional substrate," *IEEE Electron Device Lett.*, vol. 41, no. 12, pp. 1825–1828, Dec. 2020.

[25] T.-H. Hsu, K.-J. Tseng, and M.-H. Li, "Thin-film lithium niobate-on-insulator (LNOI) shear horizontal surface acoustic wave resonators," *J. Micromech. Microeng.*, vol. 31, no. 5, May 2021, Art. no. 054003.

[26] S. Zhang, R. Lu, H. Zhou, S. Link, Y. Yang, Z. Li, K. Huang, X. Ou, and S. Gong, "Surface acoustic wave devices using lithium niobate on silicon carbide," *IEEE Trans. Microw. Theory Techn.*, vol. 68, no. 9, pp. 3653–3666, Sep. 2020.

YIWEN YAO received the B.S. degree from Tianjin Normal University, Tianjin, China, in 2019. She is currently pursuing the M.S. degree with Xiamen University, Xiamen, China.

Her current research interests include computational electromagnetics, with a focus on the surface acoustic wave.

MINGWEI ZHUANG (Member, IEEE) received the B.S. degree in applied physics from the University of Shandong Jiaotong of China, Jinan, China, in 2011, and the Ph.D. degree in radiophysics from the Institute of Electromagnetics and Acoustics, Xiamen University, Xiamen, China, in 2019.

From 2016 to 2017, he was a Visiting Student with the Department of Electrical and Computer Engineering, Duke University, Durham, NC, USA. His research interests include numerical methods in acoustics, electromagnetics, and the multiphysics field.

JUNHUI CHEN received the B.S. degree in engineering from Hubei Normal University, China, in 2019. He is currently pursuing the M.S. degree with Xiamen University, China.

His research interests include computational electromagnetism, focusing on the fast and effective solution of field circuit coupling problems.

KE CHEN (Member, IEEE) received the B.S. degree in industrial engineering and the M.S. degree in mechanical engineering from the University of Electronic Science and Technology of China, Chengdu, China, in 2013 and 2016, respectively, and the Ph.D. degree in the electromagnetic field and microwave technology from Xiamen University, in 2020.

She is currently a Postdoctoral Researcher with Xiamen University. Her research interests include computational electromagnetics, IC simulation, and multiscale computing.

QING HUO LIU (Fellow, IEEE) received the B.S. and M.S. degrees in physics from Xiamen University, Xiamen, China, in 1983 and 1986, respectively, and the Ph.D. degree in electrical engineering from the University of Illinois at Urbana–Champaign, Champaign, IL, USA, in 1989.

He was a Research Assistant with the Electromagnetics Laboratory, University of Illinois at Urbana–Champaign, from September 1986 to December 1988, where he was a Postdoctoral Research Associate, from January 1989 to February 1990. He was a Research Scientist and a Program Leader with Schlumberger-Doll Research, Ridgefield, CT, USA, from 1990 to 1995. From 1996 to May 1999, he was an Associate Professor with New Mexico State University, Las Cruces, NM, USA. From 1999 to 2022, he was a tenured Full Professor of electrical and computer engineering with Duke University, Durham, NC, USA. He is currently a Chair Professor with the Eastern Institute for Advanced Study and a Visiting Chair Professor with Xiamen University. His research interests include computational electromagnetics and acoustics, inverse problems, and their applications in nanophotonics, geophysics, biomedical imaging, and electronic design automation. He has published widely in these areas.

Dr. Liu is a fellow of the Optical Society of America, the Acoustical Society of America, and the Electromagnetics Academy. He received the 1996 Presidential Early Career Award for Scientists and Engineers (PECASE) from the White House, the 1996 Early Career Research Award from the Environmental Protection Agency, the 1997 Career Award from the National Science Foundation, the 2017 Technical Achievement Award, the 2018 Computational Electromagnetics Award from the Applied Computational Electromagnetics Society, the 2018 Harrington-Mittra Award in Computational Electromagnetics from the IEEE Antennas and Propagation Society, and the University of Illinois at Urbana–Champaign ECE Distinguished Alumni Award, in 2018. He served as an IEEE Antennas and Propagation Society Distinguished Lecturer and the Founding Editor-in-Chief for the IEEE JOURNAL ON MULTISCALE AND MULTIPHYSICS COMPUTATIONAL TECHNIQUES, from 2015 to 2018.